Low-energy electronic structure of perovskite and Ruddlesden-Popper semiconductors in the Ba-Zr-S system probed by bond-selective polarized x-ray absorption spectroscopy, infrared reflectivity, and Raman scattering

Kevin Ye, Nathan Z. Koocher, Stephen Filippone, Shanyuan Niu, Boyang Zhao, Matthew Yeung, Sharon Bone, Adam J. Robinson, Patrick Vora, André Schleife, Long Ju, Alexey Boubnov, James M. Rondinelli, Jayakanth Ravichandran, and R. Jaramillo

Phys. Rev. B **105**, 195203 — Published 11 May 2022

DOI: 10.1103/PhysRevB.105.195203

Low-energy electronic structure of perovskite and Ruddlesden-Popper semiconductors in the Ba-Zr-S system probed by bond-selective polarized X-ray absorption spectroscopy, infrared reflectivity, and Raman scattering

Kevin Ye[1], Nathan Z. Koocher[2], Stephen Filippone[1], Shanyuan Niu[3†], Boyang Zhao[3], Matthew Yeung[4], Sharon Bone[5], Adam J. Robinson[6], Patrick Vora[6], André Schleife[7], Long Ju[8], Alexey Boubnov[9], James M. Rondinelli[2], Jayakanth Ravichandran[3], R. Jaramillo[1‡]

1. Department of Materials Science and Engineering, Massachusetts Institute of Technology, Cambridge, MA 02139, USA

2. Department of Materials Science and Engineering, Northwestern University, Evanston, IL 60208, USA

3. Mork Family Department of Chemical Engineering and Materials Science, University of Southern California, Los Angeles, California 90089, USA

4. Department of Electrical Engineering and Computer Science, Massachusetts Institute of Technology, Cambridge, MA 02139, USA

5. Stanford Synchrotron Radiation Lightsource, SLAC National Accelerator Laboratory, Menlo Park, CA 94025, USA

6. Department of Physics and Astronomy and Quantum Science and Engineering Center, George Mason University, Fairfax, VA 22030, USA

7. Department of Materials Science and Engineering, Materials Research Laboratory, and National Center for Supercomputing Applications, University of Illinois at Urbana-Champaign, Urbana, IL 61801, USA

8. Department of Physics, Massachusetts Institute of Technology, Cambridge, MA 02139, USA

9. Institute of Nanotechnology, Karlsruhe Institute of Technology, Eggenstein-Leopoldshafen, 76344, Germany

† *Present address: Department of Materials Science and Engineering, Nanjing University, Nanjing, China.*

‡ *email address: rjaramil@mit.edu*

Abstract

Chalcogenides in the perovskite and the related, layered Ruddlesden-Popper crystal structures ("chalcogenide perovskites" for brevity) are an exciting family of semiconductors, but remain experimentally little-studied. Chalcogenide perovskites share crystal structures and some physical properties with ionic compounds such as oxide and halide perovskites, but the metal-chalcogen bonds responsible for semiconducting behavior are substantially more covalent than in these more-studied perovskites. Here we use complementary experimental and theoretical methods to study how the mixed ionic-covalent Zr-S bonds support the electronic structure and physical properties of perovskite $BaZrS_3$ and Ruddlesden-Popper $Ba_3Zr_2S_7$. We apply theoretical methods to assign

features to experimentally measured X-ray absorption spectroscopy (XAS) to particular orbital transitions, enabling a clear physical interpretation of angle-dependent, polarized XAS data measured on single crystal samples, and an atomistic view of the covalent bonding network that facilitates charge transport. Polarized Raman measurements identify signatures of crystalline anisotropy in $Ba_3Zr_2S_7$ and enable the first assignments of mode symmetry in this material. IR reflectivity reveals electronic transport properties that augur well for the use of chalcogenide perovskites in optoelectronic and energy-conversion technologies.

1. Introduction

Solid state chemistry underpins the usefulness of semiconductors. Details of structure and bonding determine the band gap and opto-electronic properties, and are the starting points for understanding doping and electronic transport. For materials with both covalent and ionic bonding characteristics, the balance between covalent and ionic bonding has outsized influence on the electronic structure near the conduction and valence band extrema – *i.e.*, the "low-energy" electronic structure that determines band-edge optical absorption and electronic transport mobility. Experimental probes of this low-energy structure can be particularly helpful in trying to understand structure-property relationships.

Chalcogenides in the perovskite and related, Ruddlesden-Popper structure types (here referred to collectively as "chalcogenide perovskites" for brevity) are gaining increased attention as a class of emerging semiconductors with outstanding optoelectronic properties [1–8]. Chalcogenide perovskites feature band gap (E_g) tunable from teal ($E_g \approx 2.5$ eV) through the infrared (IR), they have strong optical absorption and luminescence, and results from several groups suggest inherently slow non-radiative electron-hole recombination [4,6–10]. Chalcogenide perovskites are comprised of inexpensive and non-toxic elements, and are thermally very stable, which bode well for future widescale manufacturing and deployment, for instance in thin-film solar cells [11,12]. We have identified chalcogenide perovskites as semiconductors with exceptionally strong dielectric response, comparable only to lead halide perovskites among known semiconductors with band gap in the visible and near-infrared (VIS-NIR) [13,14]. In recent work, we have achieved first-of-a-kind synthesis of large-area, atomically-smooth, epitaxial thin films of $BaZrS_3$ by pulsed laser deposition (PLD) and molecular beam epitaxy (MBE) [15,16].

In this work, we address the relationship between crystal structure and the low energy electronic structure in chalcogenide perovskites in the Ba-Zr-S system. $BaZrS_3$ (space group 62, *Pnma*) forms in a distorted-perovskite crystal structure (**Fig. 1a-b**). $Ba_3Zr_2S_7$ (space group 136, $P4_2/mnm$) is one of the Ruddlesden-Popper homologous series $Ba_{n+1}Zr_nS_{3n+1}$, featuring perovskite-like layers with $n = 2$ corner-sharing ZrS_6 octahedra separated by rock salt-like, Ba-rich layers (**Fig. 1c-d**). For oxides and halides, the band gap increases upon moving from fully-connected ZrS_6 octahedra in the perovskite ($n = \infty$) structure to confined layers in the Ruddlesden-Popper structures; this effect is commonly ascribed to quantum confinement of the electron wavefunctions within the perovskite-like layers. However, we have shown that this trend is violated by the chalcogenide perovskites: $BaZrS_3$ has a band gap of 1.83 eV, whereas $Ba_3Zr_2S_7$ and Ba_2ZrS_4 have band gap of 1.28 and 1.33 eV, respectively (the band gap of $Ba_3Zr_2S_7$ is indirect, but a direct transition at 1.35 eV makes it a strong absorber in the NIR) [10]. This peculiar behavior derives from octahedral tilts and the Zr-S-Zr bond angle, which becomes straighter (*i.e.*, closer to 180°) in the Ruddlesden-Popper structures than in the perovskite structure. This bond-angle-dependence of the semiconducting properties points to the importance of directional, covalent bonding in determining the low-energy electronic structure.

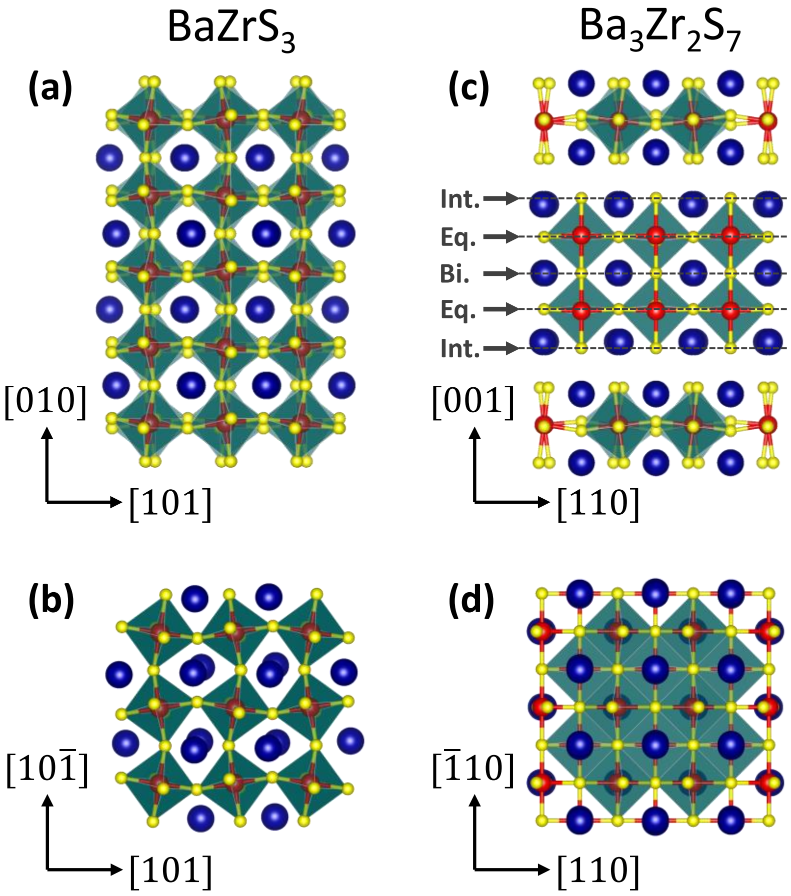

Figure 1: Crystal structures of $BaZrS_3$ (a, b) and $Ba_3Zr_2S_7$ (c, d) shown in orthographic projection; barium (blue), zirconium (red), and sulfur (yellow). Zr-S bonds are shown as connected red and yellow cylinders. The Zr-S-Zr bond angles in $Ba_3Zr_2S_7$ are closer to 180° than are the Zr-S-Zr bonds in $BaZrS_3$, which explains differences in the low-energy electronic structure, including the band gap. The labels in (c) indicate layers of distinct sulfur sites: interface (int.), equatorial (eq.), and bilayer (bi.).

Here we use a combination of X-ray absorption spectroscopy (XAS), non-contact electronic transport (*i.e.* IR reflectivity), polarized Raman spectroscopy, and electronic structure theory to probe and interpret the effects of mixed ionic-covalent bonding and layered crystal structures on the semiconducting properties of materials in the Ba-Zr-S system. Our XAS measurements, including polarization-dependent studies on single crystals, and supported by theory, highlight the covalent interactions that determine the low-energy electronic structure and are responsible for good charge transport mobility. Our transport measurements suggest that chalcogenide perovskites have among the highest room-temperature mobility reported to-date among perovskite-structured semiconductors (including halides and oxides). Polarized Raman spectroscopy reveals anisotropic low wavenumber modes, enables the first mode symmetry assignments, and identifies which modes are likely to contribute most strongly to polaron formation.

2. Methods

2.1. Experimental methods

We prepared samples following previously-reported procedures [9,17]. We made powder samples by solid state reaction, with iodine as a catalyst. Barium sulfide powder (Sigma-Aldrich 99.9%), zirconium powder (STREM, 99.5%), sulfur pieces (Alfa Aesar 99.999%), and iodine pieces (Alfa Aesar 99.99%) were stored and handled in a nitrogen-filled glovebox. We ground stoichiometric quantities of precursors, with a total weight of 1 g, and loaded them along with 0.5 $mg\cdot cm^{-3}$ of iodine into a quartz tube with a diameter of ¾″, working entirely inside a glove box. For $Ba_3Zr_2S_7$, the precursors were synthesized $BaZrS_3$ powder with added BaS. We capped the tube with Ultra-Torr fittings (Swagelok) and a needle valve before removing from the glove box, to avoid air exposure. We then evacuated the tube to 10 mbar and sealed it using a natural gas blowtorch. $BaZrS_3$ ($Ba_3Zr_2S_7$) were formed by heating to 960 (1050) °C at a rate of 1.6 °C/min, and held for 100 (40) hrs, then quenched to room temperature using a sliding furnace setup with a cooling rate higher than 100 °C/min. We grew crystals using the flux method. We ground and mixed 1 g of $BaCl_2$ powder (Alfa Aesar, 99.998%) together with 0.5 g of stoichiometric mixtures of precursor powders (BaS, Zr, and S), and loaded the resulting powder into a quartz tube, as for powder synthesis. For $BaZrS_3$ crystal growth we heated to 1050 °C at a rate of 1.6 °C/min, held at 1050 °C for 100 hrs, cooled to 800 °C at a rate of 0.1 °C/min, and then cooled to room temperature in an uncontrolled manner by shutting off the furnace. To make $Ba_3Zr_2S_7$ crystals we heated to 1050 °C at a rate of 0.3 °C/min, held at 1050 °C for 40 hrs, cooled to 400 °C at a rate of 1 °C/min, and then cooled to room temperature uncontrolled. The samples obtained we washed repeatedly with deionized water and isopropyl alcohol to remove excess flux before drying in airflow.

We measured S K-edge and Zr $L_{2,3}$-edge X-ray near edge absorption structure (XANES) spectra at beamline 14-3 at the Stanford Synchrotron Radiation Lightsource using a Si(111) double crystal monochromator. The beam was focused to a 5 μm spot using a set of KB-mirrors. We mounted samples inside a He atmosphere at room temperature. The monochromator was calibrated by setting the first peak in the spectrum of $Na_2S_2O_3$ to 2472.02 eV. We prepared powder samples by preparing thin coatings on low-sulfur tape, which were mounted in the beam on a motorized multi-sample stage. We measured XAS in fluorescence-yield mode. For powder samples we used a Lytle type detector, and for single crystals we used a Vortex four-element Si drift detector. We normalized the detector signal by the incident beam intensity as measured by an upstream ionization chamber. We measured polarization-dependent data on single crystals that were mounted on a rotation stage, to control the angle between the crystal axes and the synchrotron radiation, which is highly-polarized from the bending magnet source. For all spectra, we performed background subtraction and step-edge normalization by fitting a straight line to the pre-edge region (between 2440 and 2460 eV for the S K-edge, between 2270 and 2300 eV for the Zr $L_{2,3}$-edge) and a second-order polynomial to the post-edge region (between 2490 and 2515 eV for S K-edge, between 2320 and 2350 eV for Zr $L_{2,3}$-edge). We performed data processing using Athena, contained within the Demeter 0.9.24 package [18].

We performed IR reflectivity and Raman spectroscopy measurements on oriented and polished $Ba_3Zr_2S_7$ single crystals. We mounted crystals in epoxy (Pace Technologies, Ultrathin 2 Low Viscosity Resin) and thinned them by grinding and polishing to 25 μm thickness, which we estimated using an embedded plastic spacer. We ground using sandpaper and water lubricant down to 9 μm grit size. We polished using diamond suspensions, stepping down to 1 μm, before a final polish with a 0.25 μm silica suspension. We used X-ray diffraction (XRD) to determine crystal orientation before mounting, and repeated XRD measurements after polishing to quantify any unintended miscuts.

We performed mid-IR reflectivity measurements in a visible-pump, IR-probe experimental setup. We measured the change in reflectivity ($\Delta R/R$) of a linearly-polarized IR probe pulse after a carrier-generation pump pulse. The pump was a linearly-polarized 215 fs-wide pulse at 515 nm, generated through second harmonic generation from a 1030 nm laser, with a repetition rate of 1 MHz. The pump had a per-pulse fluence of 0.0819 μJ/cm^2. The probe beam was a linearly-polarized (p-polarized) pulse at 9.5 μm, generated in silver thiogallate ($AgGaS_2$) through the difference frequency generation process by nonlinear mixing of pulses at 1.3 μm and 1.5 μm from an optical parametric amplifier (Light Conversion Orpheus-F). The probe pulse width was estimated to be < 150 fs using cross-correlation measurements, and was guided to the sample at near-normal incidence. We rotated the crystal relative to the IR probe beam polarization to measure conductivity along different crystal directions.

We performed Raman spectroscopy measurements in ambient conditions using a 532 nm laser. This beam was directed through an objective lens (40× magnification, 0.6 NA), with a power of 200 μW measured before the objective. We used reflective Bragg gratings to clean the laser line for excitation and to reject it for collection. These gratings allow for features to be observed down to 20 cm^{-1} with a single spectrometer. We measured spectra using on a liquid-N_2-cooled silicon CCD camera mounted on a 0.5 m length spectrometer. We placed polarizers in the excitation and collection beam paths to achieve co- and cross-polarization conditions. We mounted the sample on a rotation stage for measurements along different crystal axes. Excitation and collection polarizers were configured in three orientations: co-polarized along [001], co-polarized along [110], and cross-polarized.

2.2. Theoretical methods

We performed density functional theory (DFT) calculations using the Vienna *Ab initio* Simulation Package (VASP), employing the PBEsol exchange correlation functional and projector-augmented wave (PAW) pseudopotentials [19–21]. The valence electron configurations for the pseudopotentials are: $5s^2 5p^6 6s^2$ for Ba, $4s^2 4p^6 5s^1 4d^3$ for Zr, and $3s^2 3p^4$ for S. Relaxation parameters include a 600 eV plane-wave cutoff energy, a 6×6×2 Γ-centered *k*-point mesh, an electronic convergence threshold of 10^{-8} eV, and an ionic force convergence threshold of 10^{-5} eV/

Å. The stress tensor for the relaxed atomic structure was less than 8.6 × 10^{-4} kbar. We broadened the resulting densities of states and spectra using Gaussian smearing with a width of 0.1 eV.

We calculated the sulfur K-edge X-ray absorption spectrum of $Ba_3Zr_2S_7$ using VASP version 6.1.1, employing a 2×2×1 supercell (the *c* lattice parameter is the long axis) with 4800 electronic bands (NBANDS tag) and the charge of the core hole set to 1.0 (CLZ tag). The formula for the dielectric function is as follows [22]:

$$\epsilon_{\alpha\beta}^{(2)}(\omega) = \frac{4\pi^2 e^2 \hbar^4}{\Omega\omega^2 m_e^2} \sum_{c,\boldsymbol{k}} 2\omega_{\boldsymbol{k}} \delta(\varepsilon_{ck} - \varepsilon_{core} - \omega) \times M_\alpha^{core\rightarrow c\boldsymbol{k}} M_\beta^{core\rightarrow c\boldsymbol{k}^*} \quad (1)$$

where α, β are cartesian directions, Ω is the cell volume, m_e is the electron mass, the sum is done over conduction bands c and k-points k, ε are orbital energies, and M are momentum matrix elements [23]. We further decomposed the optical response by angular momentum by weighting the dielectric value $\epsilon_{\alpha\beta}^{(2)}(\omega)$ calculated for a given transition by the appropriate projection p_{lmnk}^N of the wave function ϕ_{nk} on a spherical harmonic Y_{lm} for ion *N*, magnetic quantum number *m*, and orbital quantum number *l*. Following Eq. (A2) in Ref. [24], this projection operation is represented by:

$$\epsilon_{\alpha\beta}^{(2)}(\omega) = \frac{4\pi^2 e^2 \hbar^4}{\Omega\omega^2 m_e^2} \sum_{c,\boldsymbol{k}} \left(\sum_{N,l,m} p_{lmnk}^N\right) \times 2\omega_{\boldsymbol{k}} \delta(\varepsilon_{ck} - \varepsilon_{core} - \omega) \times M_\alpha^{core\rightarrow c\boldsymbol{k}} M_\beta^{core\rightarrow c\boldsymbol{k}^*} \quad (2)$$

We computed Γ-point phonons using density functional perturbation theory within VASP using PHONOPY codes [23,25,26]. The orbital-resolved band structure was generated using the BandUP code [27,28].

We also calculated XANES spectra using the FDMNES code [29,30]. Both FDMNES and VASP are based on DFT, but FDMNES is based on analysis of clusters in real space. We analyze a 7 Å cluster radius around the Zr (Zr L_2-edge) and S (S K-edge) central, absorbing atom, using reference structures for $BaZrS_3$ (*Pnma*, ICSD 23288) and $Ba_3Zr_2S_7$ (*P*4_2*/mnm*, ICSD 59271). For simulating polarized XANES spectra and densities of states (DOS) decomposed into the individual matrix elements, we generated a large spherical cluster centered around the absorbing atom, and rotated the cluster to align bonds along the Cartesian coordinates. The DOS calculated in FDMNES consists of matrix elements projected along their respective directions in a Cartesian coordinate system, but irrespective of the orientation of the chemical structure. Therefore, the alignment of the structure in space was necessary for correlation of the calculated matrix elements with the structure. For the Zr *d*-DOS, we directed one Zr-S bond along the z-direction, and one of the perpendicular bonds was confined to the yz-plane. For the sulfur DOS, we directed a S-Zr bond along the z-direction, and the perpendicular S-Ba bonds along the other two Cartesian axes.

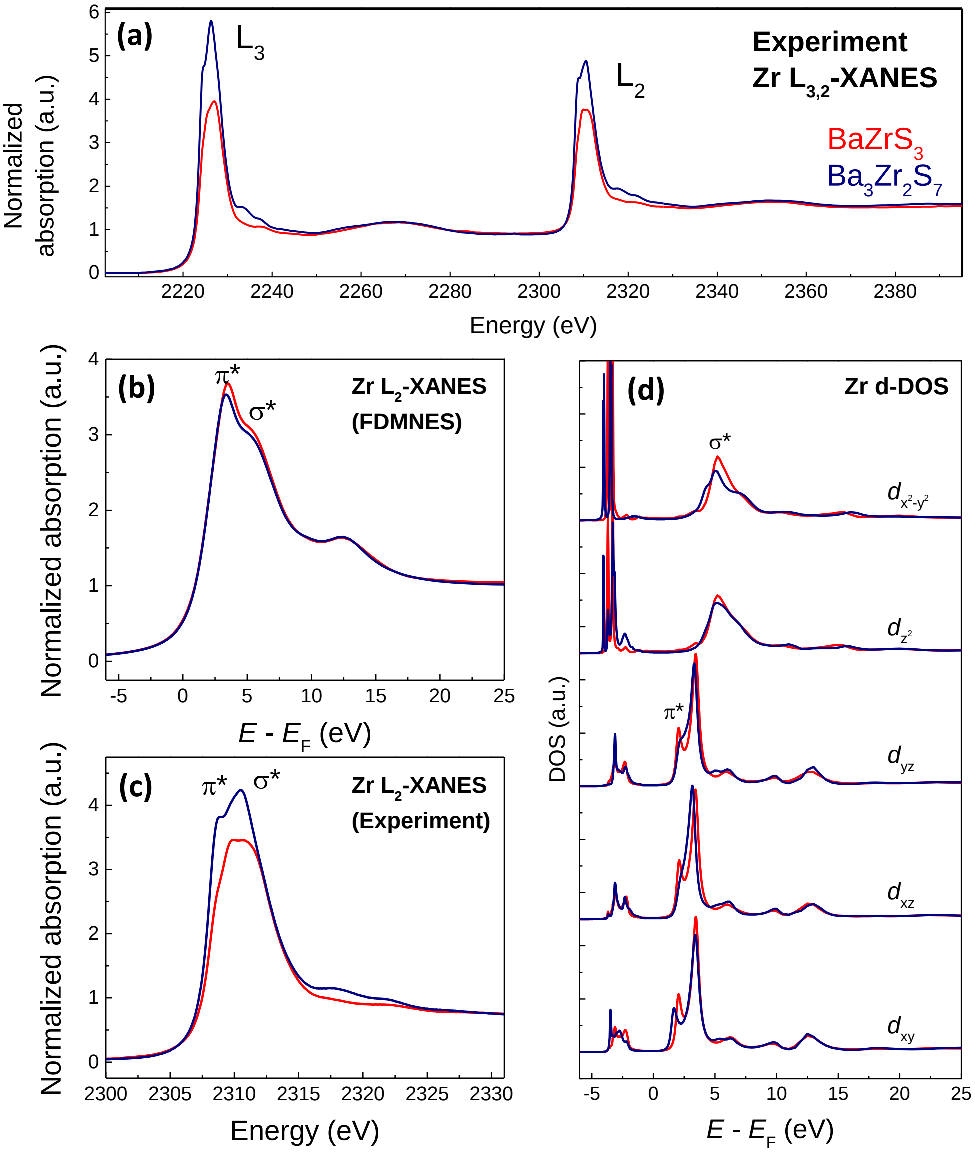

Figure 2: Zr $L_{2,3}$-edge XANES data measured on powder samples of $BaZrS_3$ and $Ba_3Zr_2S_7$ and comparison with theory. (a) Experimental data for $BaZrS_3$ and $Ba_3Zr_2S_7$. (b-c) The L_2-edge spectra as calculated by FDMNES (b) and measured experimentally (c). (d) Zr 4d DOS resolved by orbitals in the octahedral crystal field basis. In FDMNES, the Fermi level (E_F) is defined as the origin of the energy scale. In all panels, data for the two phases are colored as labeled in (a).

3. Results: X-ray absorption spectroscopy

We present in **Fig. 2a** the results of XANES measurements on powder samples at the Zr $L_{2,3}$-edge. The Zr $L_{2,3}$-edge spectra represent $2p_{1/2} \rightarrow 4d_{3/2}$ and $2p_{3/2} \rightarrow 4d_{3/2}/4d_{5/2}$ transitions, respectively, explaining a higher intensity of L_3 than L_2. The L_3/L_2 intensity ratio of $Ba_3Zr_2S_7$ is higher than that of $BaZrS_3$, implying a change in relative occupancy of $4d_{3/2}$ and $4d_{5/2}$. In **Fig. 2b-c** we focus on the L_2-edge XANES spectra, experimentally measured and as calculated by

FDMNES. The L_2-edge is comprised of two peaks, which we attribute to π^* and σ^* bonds (technically, antibonding molecular orbitals do not represent bonds; here we use terminology "π^* bonds" and "σ^* bonds" to indicate molecular orbital overlaps). The theoretically-calculated XANES data do not reproduce the observed intensity ratio of the two main features, or accurately account for the intensity differences between the spectra of $BaZrS_3$ and $Ba_3Zr_2S_7$, especially of the feature at 2320 eV. Given the limitations of the code causing such quantitative inaccuracies, we focus mainly on the energy positions, especially in the densities of states, to qualitatively explain the electronic structure. In **Fig. 2d** we present the Zr 4d DOS resolved by orbitals in the octahedral crystal field basis. The energy scale is relative to the Fermi level (E_F), making the DOS of both structures directly comparable. The conduction band edge is comprised of π^* bonds involving the t_{2g} orbitals d_{yz}, d_{xz}, and d_{xy}. The e_g orbitals d_{z^2} and $d_{x^2-y^2}$ are higher in energy and form σ^* bonds. The antibonding character is revealed by crystal orbital occupation population (COOP) analysis (not shown) [31]. Looking in fine detail, we see that the lowest-energy portion of the conduction band edge has d_{xy} character, and appears at lower energy in $Ba_3Zr_2S_7$ than in $BaZrS_3$, consistent with the lower band gap in the Ruddlesden-Popper phase.

In **Fig. 3** we focus our discussion on the powder sulfur K-edge XANES data. In **Fig. 3a** we present experimental data for $BaZrS_3$ and $Ba_3Zr_2S_7$, and in **Fig. 3b** we present XANES spectra calculated by VASP and decomposed by atomic orbital. We label the first two major peaks A and B, and we turn to theory to assign these peaks to particular orbitals. The low-energy peak (labeled A) derives from transitions to S3p - Zr4d hybridized orbitals. These are the orbitals that form Zr-S-Zr of π^* bonds within the network of corner-connected octahedra, and are most responsible for conduction-band-edge electronic transport (discussed further below). The next prominent peak (labeled B) derives most prominently from transitions to the S3p - Ba5d hydridized orbital, with some contributions also from S3p - Zr4d. In the analysis that follows, we focus on the low-energy peak A, which represents the low-energy states near the band edge that are most relevant to semiconducting properties. We note that, in the orbital decomposition analysis presented in **Fig. 3b**, the envelope of the projected orbital contributions lacks the step-like feature characteristic of the absorption spectra of isolated atoms, and that is always present in experimental data. This is because the projection operation requires partitioning, which results in some missing interstitial contributions that do appear in the total calculated spectrum, which we plot in **Fig. 3b** as a grey line (this is a common density projection problem for solids).

Hybridization between the metal orbitals and the sulfur S3p ligands that comprise the valence band edge can be estimated from the strength of the low-energy peak in the S XANES data, following the method applied by Suntivich *et al.* to transition metal oxides [32]. This analysis assumes that all of the S3p - Zr4d hybridized orbitals are equivalent, with the same extent of hybridization and constant matrix elements. With this simplifying assumption, the spectral intensity of this low-energy peak is linearly proportional to the density of empty S3p - Zr4d hybridized orbitals. That is, the relative hybridization of S3p - Zr4d between phases can be estimated by comparing the term $(1/h_{4d})I_{\text{hyb}}$, where I_{hyb} is the background-corrected spectral intensity of the low-energy peak, and h_{4d} is the number of empty S3p - Zr4d states per sulfur atom. Since the formal oxidation states are the same for $BaZrS_3$ and $Ba_3Zr_2S_7$, h_{4d} = 3.33 for $BaZrS_3$ and h_{4d} = 2.86 for $Ba_3Zr_2S_7$. We estimated I_{hyb} by subtracting a linear background, determined by adjacent local minima (**Fig. 3b**). We find that $(1/h_{4d})I_{\mathrm{hyb}}$ is 1.65 for $BaZrS_3$ and 1.75 for $Ba_3Zr_2S_7$. The increased covalency for $Ba_3Zr_2S_7$ compared to $BaZrS_3$ is consistent with the band gap trend and the differences in Zr-S-Zr bond angles (**Fig. 1**) [10].

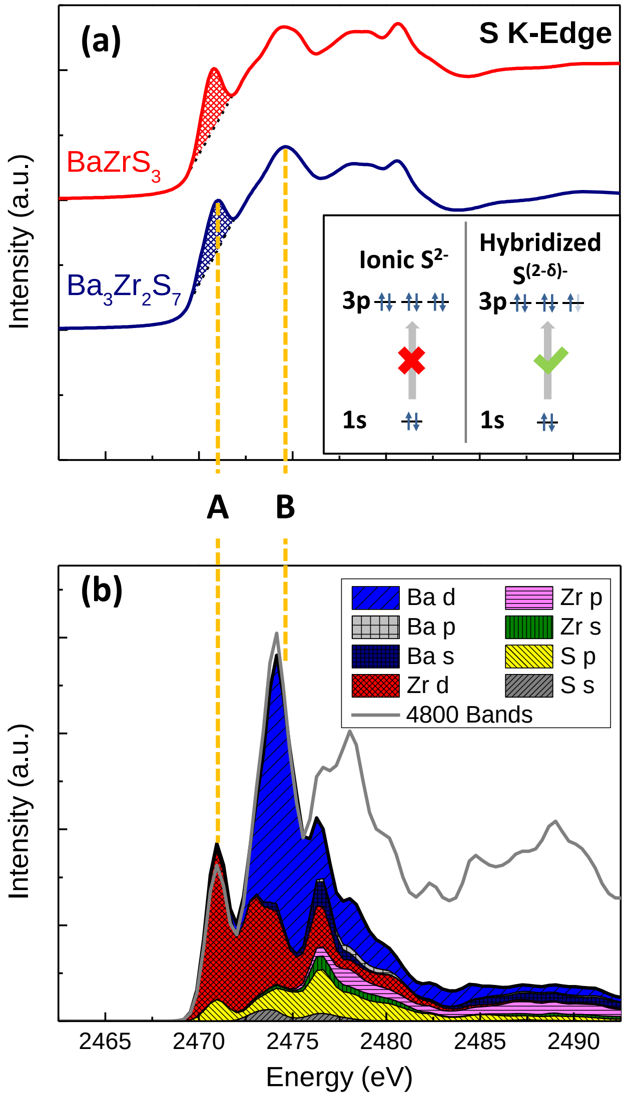

Figure 3: Sulfur K-edge XANES data measured on powder samples of $BaZrS_3$ and $Ba_3Zr_2S_7$ and comparison with theory. (a) S K-edge. The inset illustrates the role of metal-sulfur hybridization in generating the low-energy peak near 2472 eV. (b) Theoretical XANES spectrum for $Ba_3Zr_2S_7$ (powder sample average) decomposed by atomic orbitals, allowing us to interpret the experimental data. The individual contributions are presented as a cumulative plot, so that the envelope approximates the XANES spectrum. Peak A derives from transitions to S3p - Zr4d hybridized orbitals, as illustrated in the inset to panel (a). Peak B derives from transitions to higher-lying Ba5d orbitals. The envelope of the projected orbital contributions lacks the step-like feature characteristic of the absorption spectra. This is because the projection operation requires partitioning, which results in

some missing interstitial contributions that do appear in the total calculated spectrum, which we plot as a grey line.

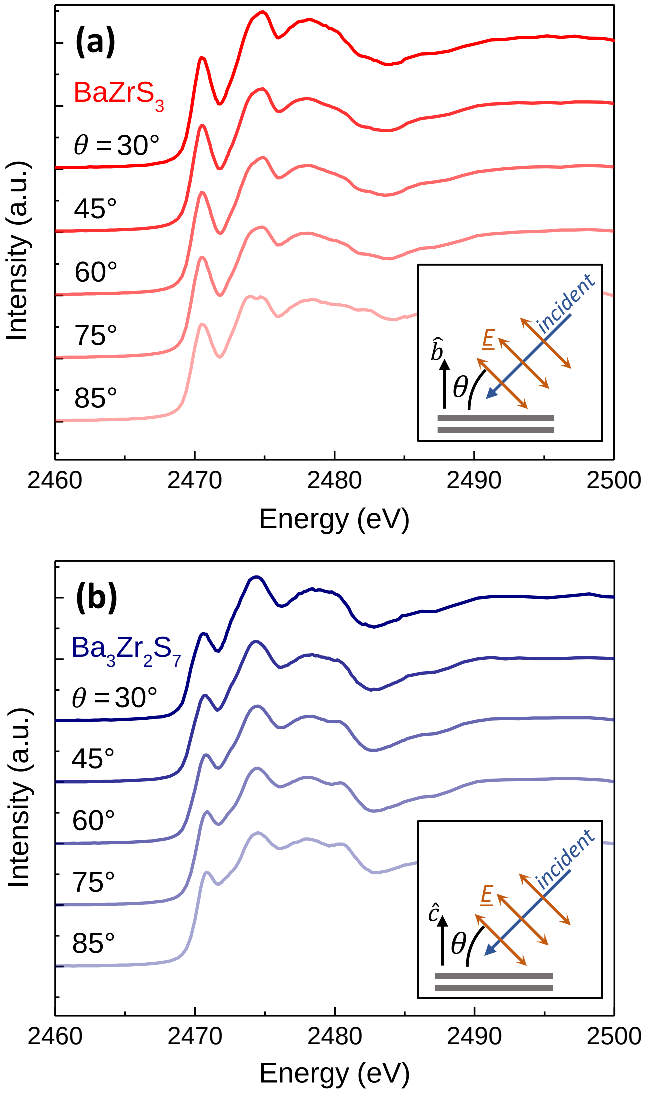

Figure 4: Polarized S K-edge XANES measurements with varying θ, the angle between X-ray electric field vector ($\underline{E}$) and the sample surface, with crystallographic orientation as illustrated in the insets. Measurements on $BaZrS_3$ and $Ba_3Zr_2S_7$ are presented in (a) and (b), respectively; data with varying θ are offset vertically for clarity.

The crystal structures of $BaZrS_3$ and $Ba_3Zr_2S_7$ suggest that Zr-S bonds within the layers of $Ba_3Zr_2S_7$ are more covalent, and it is these bonds that determine the low-energy electronic structure. To further test this hypothesis, we turn to polarized XANES, taking advantage of the polarization of synchrotron radiation. In polarized XANES the angles between the X-ray electric field vector ($\underline{E}$) and the crystal axes are controlled (**Fig. 4**). Within the dipole approximation, polarized XANES allows experimental study of how the core-valence transition strength varies with the transition dipole moment. In **Fig. 4** we present the S K-edge data for $BaZrS_3$ and $Ba_3Zr_2S_7$

for varying angle θ, which we define as the angle between $\underline{E}$ and the exposed crystal surface. For $BaZrS_3$, the exposed surface is either (101) or (020); both are pseudo-cubic faces, and we draw **Fig. 4a** for the case of an (020) surface. For $Ba_3Zr_2S_7$, the exposed surface is the (001) basal plane, so that θ is the angle between the X-ray incident direction and the long axis $\hat{c}$. We assume that sample rotation around the surface normal is of minor importance; this is justified for pseudo-cubic $BaZrS_3$ and tetragonal $Ba_3Zr_2S_7$.

The low-energy peak in the S K-edge spectrum contains information about the low-energy electronic structure at the conduction band edge. Looking carefully at this data (**Fig. 5a**), we see that both the intensity and the shape of the low-energy peak varies with θ for $Ba_3Zr_2S_7$, whereas the intensity variation is less and the shape is constant for $BaZrS_3$. As θ approaches 0° ($\underline{E}$ in the basal plane), this peak for $Ba_3Zr_2S_7$ develops a low-energy shoulder, which we label as A´. This feature is suggestive of hybridized Zr-S bonds in the basal plane forming the conduction band edge. The low-energy peak, including this shoulder, appears at lower energy for $Ba_3Zr_2S_7$ than for $BaZrS_3$, consistent with the lower band gap in the Ruddlesden-Popper than in the perovskite phase (1.3 and 1.8 eV, respectively).

To connect the polarized XANES experimental data to the low-energy electronic structure in finer detail, we turn to theory. Theoretical methods can predict polarization-dependent XANES spectra, which are equivalent to the imaginary part of the dielectric tensor. Together, experimental and theoretical XANES data can directly identify which orbitals, bonds, and bands contribute most to the low-energy electronic structure. In **Fig. 5b-e**, we calculate the contributions of discrete sulfur sites to the polarization-dependent XANES spectrum, simulating the same set of angles (θ) as in the experimental data in **Fig. 5a**. We label two notable features in the experimentally-measured and theoretically-calculated S K-edge spectra, labeled A' and A. As θ increases, A' is suppressed and peak A moves to higher energy. In **Fig. 5f, g** we show the representative contribution of each sulfur site to the theoretically-calculated total S K-edge at the highest and lowest angles experimentally measured (30° and 85°). At both angles, the contribution from equatorial sites is larger than that from bilayer and interface sites, due to the greater number of equatorial sites in the unit cell. However, it is also apparent from the θ-dependence that the bilayer site makes the most significant contribution to the lowest-energy feature A'.

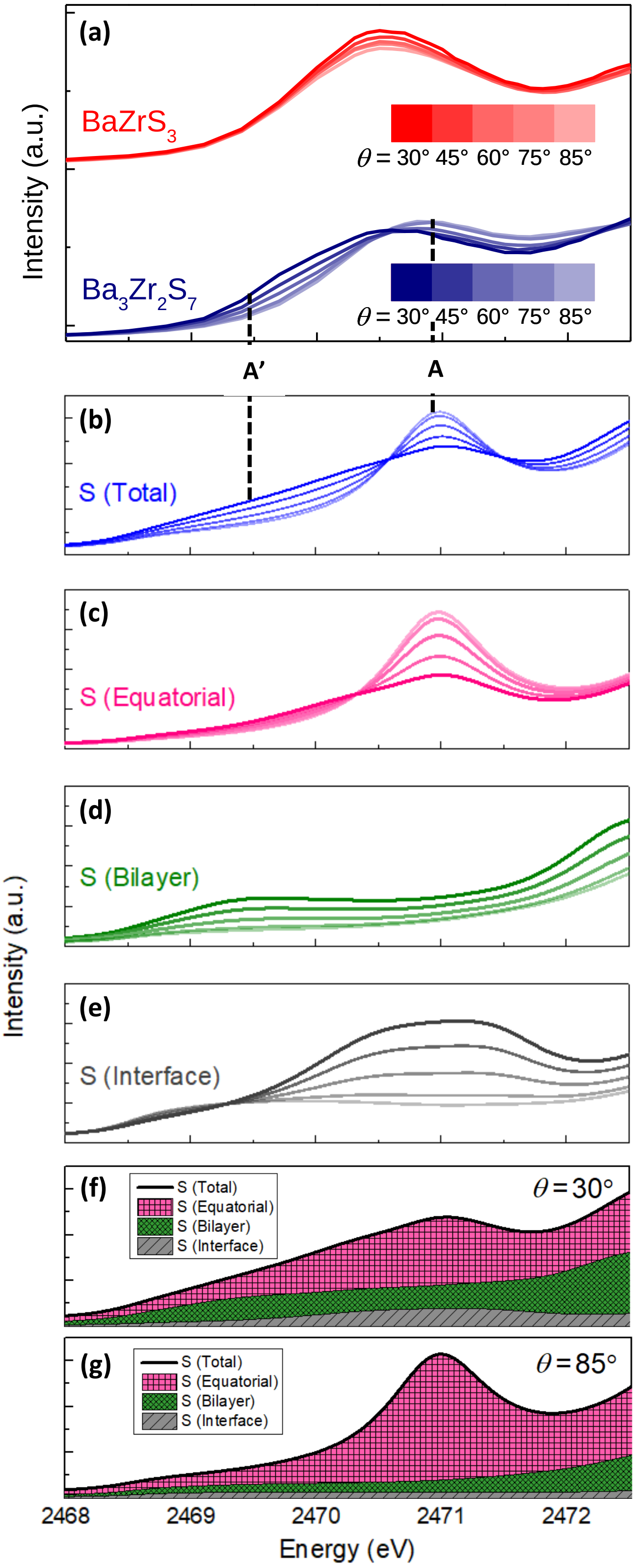
(a)
BaZrS$_3$
θ = 30° 45° 60° 75° 85°
Ba$_3$Zr$_2$S$_7$
θ = 30° 45° 60° 75° 85°
Intensity (a.u.)
A'
A
(b)
S (Total)
(c)
S (Equatorial)
(d)
S (Bilayer)
(e)
S (Interface)
Intensity (a.u.)
(f)
S (Total)
S (Equatorial)
S (Bilayer)
S (Interface)
θ = 30°
(g)
S (Total)
S (Equatorial)
S (Bilayer)
S (Interface)
θ = 85°
2468
2469
2470
2471
2472
Energy (eV)

Figure 5: Polarization-dependent S K-edge XANES experimental data and theoretical interpretation for $Ba_3Zr_2S_7$. (a) Close-up of the θ-dependence of the low-energy peak (full data range presented in Fig. 4b). (b-e) θ-dependence of the theoretically-calculated XANES data, decomposed by discrete sulfur sites; here we present (b) total, (c) equatorial, (d) bilayer, and (e) interface sulfur sites. In each of (b-e), the color intensity matches the θ series as in (a). (f, g) Theoretically calculated total XANES spectrum decomposed by sulfur sites for (f) θ = 30° and (g) θ = 85° with site contributions as shown in (b-e).

4. Results: IR reflectivity

To further study the low-energy electronic structure and properties of $Ba_3Zr_2S_7$, we used optical-pump, IR-probe experiments to measure charge transport mobility and its anisotropy along principle crystal directions. For a sample prepared with the $[1\bar{1}0]$ direction out-of-plane, there is a substantial variation in $\Delta R/R$ as the sample is rotated around $[1\bar{1}0]$, presented in **Fig. 6a**. The Drude mobility is $\mu = q\tau/m^*$; we assume that the scattering rate τ is isotropic, so that the anisotropy in $\Delta R/R$ directly reflects anisotropy in m^*. As expected, the inferred effective mass is highest (mobility is lowest) along [001], corresponding to charge transport between layers of the Ruddlesden-Popper structure. We estimate ${m^*_{[001]}}\big/{m^*_{[110]}} = 10 \pm 1.7$. For a sample prepared with [001] out-of-plane, we observe no statistically-meaningful variation in $\Delta R/R$ as the sample is rotated along [001], presented in **Fig. 6b**. This is consistent with our expectation that the mobility has square symmetry within the Ruddlesden-Popper layers.

We model the sample as a conductive thin film on a dielectric substrate, using the Drude model in the low-frequency limit. For this model,

$$\frac{\Delta R}{R_0} = 2\left(\frac{1}{n-1} - \frac{1}{n+1}\right) y_1 \tag{3}$$

where n = 2.9 is the refractive index at λ_{IR} at equilibrium, and $y_1 = Z_0 q\mu(1 - R_{\text{VIS}})2F_0$ [14]. Z_0 is the impedance of free space, q is the fundamental charge, μ is the mobility, R_{VIS} is the reflectivity at λ_{VIS}, and F_0 is the photon area density of the carrier-generation pulse. We justify this model with self-consistency calculations, including a comparison of the carrier scattering rate to the frequency of the IR illumination, and a calculation of the IR probe attenuation through the crystal (Appendix A). Using this model, we estimate $\mu_{[100]} = \mu_{[010]} = 290 \pm 20$ cm^2/V·s, and $\mu_{[001]} = 29 \pm 1$ cm^2/V·s; the uncertainties represent statistical noise in the data and sample-to-sample variation.

The carrier type responsible for the IR reflectivity is unknown. For high pump fluence and measurement times much shorter than the recombination lifetime (measured previously), it is reasonable to assume ambipolar transport [8]. Our DFT calculations predict that the ambipolar, reduced effective masses along [100] and [001] are 1.65 and 57.64, respectively (in units of the bare electron mass), with a ratio $m^*_{[001]}/m^*_{[100]} = 34.93$. The measured ratio of 10 ± 1.7 therefore suggests that DFT fails to accurately model the properties of band-edge charge carriers; electron-phonon interactions and polaron formation may be responsible for the discrepancy.

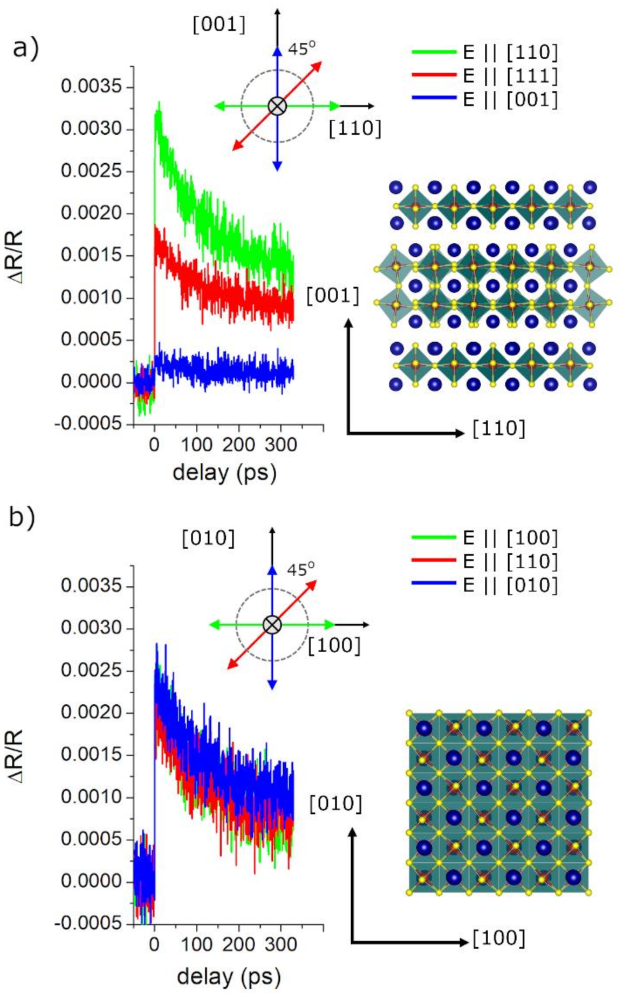

Figure 6: Normalized change in polarized IR reflectivity following an optical pump for oriented $Ba_3Zr_2S_7$ crystals. In both (a) and (b), the crystal structure is visualized as an orthographic projection along the probe beam incidence direction, and the probe beam polarization relative to the crystal axes is visualized on a compass rose. (a) Crystal oriented with the probe beam incident along $[1\bar{1}0]$. The crystal is rotated so that the IR electric field polarization ($\underline{E}$) aligns with [110] (green), [111] (red), and [001] (blue). (b) Crystal oriented with the probe beam incident along [001]. The crystal is rotated so that $\underline{E}$ aligns with [100] (green), [110] (red), and [010] (blue).

The band-to-band photoluminescence decay rate of similar $Ba_3Zr_2S_7$ crystals was measured previously [8]. In this previous work, we found that the non-radiative Shockley-Read-Hall recombination lifetime τ_{SRH} is greater than 50 ns. Using the above estimates for carrier mobility, and the Einstein relation to calculate the diffusivity (D) we find that the room-temperature ambipolar diffusion length $L = \sqrt{D\tau_{SRH}}$ is greater than 6.1 and 1.9 μm along [100] and [001], respectively. These numbers are comparable to those found in established absorbers for thin-film solar cells, and speak to the promise of chalcogenide perovskites for optoelectronic and energy conversion technologies [33,34]. However, the difference between in-plane and out-of-plane transport also speaks to the challenge of designing semiconductor devices using anisotropic materials.

5. Results: Polarized Raman spectroscopy

Polarized Raman spectroscopy on anisotropic materials can provide valuable information regarding lattice dynamics along unique axial directions. The $Ba_3Zr_2S_7$ compound is largely unexplored in this area, with only one prior study examining its properties with Raman and IR spectroscopy [35]. The tensors (***R***) for the Raman-active symmetry modes in $Ba_3Zr_2S_7$ are [36,37]:

$$\boldsymbol{R}_{\mathrm{A1g}}=\begin{pmatrix}a&0&0\\0&a&0\\0&0&b\end{pmatrix},\ \boldsymbol{R}_{\mathrm{B1g}}=\begin{pmatrix}c&0&0\\0&-c&0\\0&0&0\end{pmatrix},\ \boldsymbol{R}_{\mathrm{B2g}}=\begin{pmatrix}0&d&0\\d&0&0\\0&0&0\end{pmatrix},\ \boldsymbol{R}_{\mathrm{Eg}}=\begin{pmatrix}0&0&-e\\0&0&0\\-e&0&0\end{pmatrix}\qquad(4)$$

The variables a, b, c, d, and e are the complex components of the Raman tensor. We measure a crystal prepared with the [110] and [001] directions in-plane, as in the above IR reflectivity experiments, and we align our laboratory coordinate system with high-symmetry directions of the crystal as in **Fig. 6a**: the laboratory vertical axis is along the crystal [001] direction (normal to the basal plane), and the horizontal axis is along the crystal [110] (within the basal plane). We measure in a backscattering configuration.

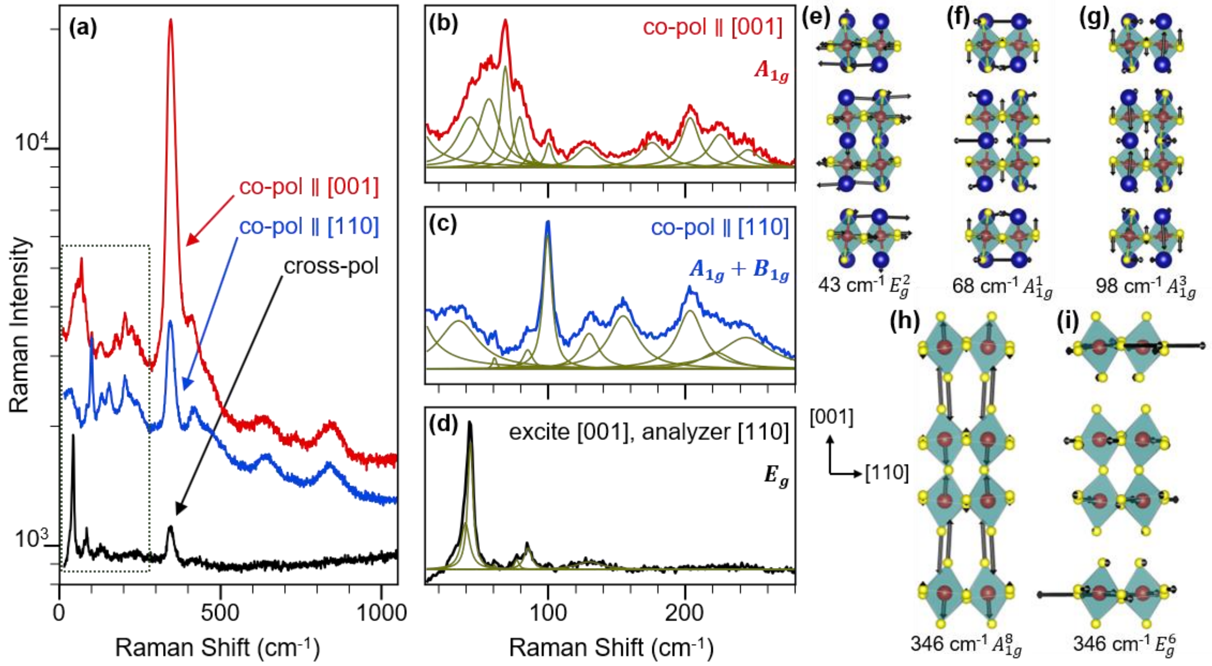

Figure 7: Polarization-resolved Raman spectra of a $Ba_3Zr_2S_7$ crystal at 300 K; the crystal is prepared as in Fig. 5a, with [001] and [110] directions in the exposed surface. (a) Co-polarized Raman spectra along [001] (red curve) and [110] (blue curve). The cross-polarized spectrum (black) was acquired with the laser polarized along [001] and the analyzer along [110]. The low frequency region (dashed box) is magnified in (b-d) for the co-polarized [001], [110], and cross-polarized spectra, respectively, with a polynomial

background subtracted. The olive lines represent individual components of multi-Lorentzian fit to each spectrum, and the mode symmetries are indicated within each panel. (e-g) Atomic displacements for the dominant low wavenumber mode in panels (b-d), respectively. (h,i) Atomic displacements for the nearly-degenerate A_{1g} and E_g modes at 346 cm^{-1} , respectively. Crystallographic orientation for atomic displacements is indicated in the figure. For these higher-frequency modes we omit the Ba atoms for clarity, to emphasize the ZrS$_6$ octahedra distortions and because the Ba atoms hardly move.

The Raman intensity (I) is given by the tensor product with the incoming ($\vec{E}_{\text{in}}$) and outgoing ($\vec{E}_{\text{out}}$) electric field vectors

$$I = \left|\vec{E}_{\text{out}} \cdot \boldsymbol{R}\vec{E}_{\text{in}}\right|^2, \tag{5}$$

where $\vec{E}$ is along [001] or along [110]. Calculating I using the tensors in Eq. 4, we find that A_{1g}, B_{1g}, and E_g modes are observable in a backscattering configuration, while B_{2g} modes are not. A_{1g} modes are visible in co-polarized measurements along [110] and [001] orientations, with intensities proportional to $|a|^2$ and $|b|^2$, respectively. B_{1g} modes are visible in co-polarized measurements along [110], and E_g modes are observable in the cross-polarized configuration.

Theory (cm^{-1})	Symmetry	Experiment (cm^{-1})	Symmetry	Ishii *et al.* (1993) (cm^{-1})
		35	Unidentified	
37	E_g	40	E_g^1	
46	E_g	43	E_g^2	42
58	B_{1g}	61	B_{1g}^1	61
69	A_{1g}	69	A_{1g}^1	
75	B_{1g}	-	-	
78	E_g	77	E_g^3	
79	B_{1g}	-	-	
81	A_{1g}	79	A_{1g}^2	
86	E_g	85	E_g^5	83
98	A_{1g}	100	A_{1g}^3	
111	A_{1g}	-	-	
127	A_{1g}	128	A_{1g}^4	129
144	B_{1g}	155	B_{1g}^2	
148	A_{1g}	-	-	
163	A_{1g}	-	-	
-	-	176	?	177
197	A_{1g}	204	A_{1g}^5	208
206	B_{1g}	-	-	
218	A_{1g}	225	A_{1g}^6	
236	A_{1g}	246	A_{1g}^7	
246	B_{1g}	-	-	
346	A_{1g}	346	A_{1g}^8	346
346	E_g	345	E_g^6	

413	A_{1g}			414

Table 1: Experimentally-observed and theoretically-predicted Raman-active single-phonon mode frequencies and symmetries. Mode symmetries are enumerated with superscripts for experiment observations. A comparison to previously observed mode frequencies agrees well with our results [35].

In **Fig. 7a**, we present results of Raman measurements co-polarized along [001] (red curve), co-polarized along [110] (blue curve), and cross-polarized (black curve). The low-wavenumber region ($\omega < 300$ cm^{-1}) is particularly feature-rich, illustrating the crystalline anisotropy. We magnify this region in **Fig. 7b-d** for the [001], [110], and cross polarized spectra respectively. The green curves are the results from multi-Lorentzian fits to the data and provide the mode frequencies shown in **Table 1**. While there are minor differences between 110-300 cm^{-1}, we find sharp peaks unique to each polarization configuration at 43 cm^{-1} (E_g^2), 68 cm^{-1} (A_{1g}^1), and 100 cm^{-1} (A_{1g}^3). Atomic displacements for these modes are shown in **Fig. 7e-g**, respectively. Each plane of Ba atoms for the E_g^2 mode alternates its character between large displacements along [110] and smaller displacements along [001]. The Zr-S octahedra solely exhibits displacements within the basal plane, which each layer out of phase with the adjacent ones. The Zr-S octahedra for the A_{1g}^1 mode undergo small displacements along [110], except for the S atoms connecting octrahedra, which show large displacements along [001]. The Ba atoms in this case show very large displacements that are entirely within the basal plane. Finally, the A_{1g}^3 mode Zr-S octahedra exhibit both in-plane and out-of-plane shear due primarily to S displacements. Ba layers within the basal plane again alternate between large displacements along [001] and smaller ones along [110].

The most prominent feature in all three spectra is the mode at 346 cm^{-1}. DFT calculations report two near-degenerate modes at this frequency, with A_{1g} and E_g symmetry. This peak is remarkably intense in the [001] spectrum, five times more so than in the [110] spectrum, and is assigned A_{1g} character. The intensity difference cannot arise from crystalline anisotropy because the optical absorption at 532 nm does not depend strongly on orientation [8]. The most likely origin is a difference between a and b in the A_{1g} Raman tensor (Eq. 4). This feature also appears in the cross-polarized spectrum, where it may be a combination of E_g symmetry and systematic error (*i.e.*, leakage) due to imperfect polarization rejection. Atomic displacement diagrams in **Fig. 7h** indicate the A_{1g}^8 mode arises from Zr-S stretching along the [001] direction. The E_g^6 mode is shown in **Fig. 7i** and involves shearing of the Zr-S octahedra along [110]. The Ba atoms in both cases remain stationary due to their larger mass.

Chalcogenide perovskites are highly-polarizable semiconductors [14]. By analogy with other highly-polarizable materials with similar crystal structures, including oxides and lead halides, it may be expected that charge carriers at the band edges form polarons [38]. The large mobility values determined above imply that polarons, if they exist in $Ba_3Zr_2S_7$, are large (*i.e.*, Fröhlich) and at room temperature are in the coherent transport regime. The Fröhlich Hamiltonian model for large polarons is often analyzed assuming a characteristic longitudinal optical (LO) phonon responsible for polaron formation, but other types of phonons may also contribute (*i.e.*, transverse optical). For chalcogenide perovskites, electronic states at the conduction band edge are strongly coupled to distortions to ZrS_6 octahedra and the Zr-S-Zr bond angles [10]. Phonons that affect the octahedra and bond angles are likely to be strongly-coupled to band-edge states and contribute to polaron formation. In particular, the prominent A_{1g}^{8} and E_g^{6} modes visualized in **Fig. 7h-i** significantly distort and twist the octahedra, respectively. Further theoretical and experimental work may quantify mode-selective electron-phonon coupling, to parameterize a Fröhlich Hamiltonian analysis particular to chalcogenide perovskites.

In **Table 2** we summarize the modes appearing above 450 cm^{-1}. There are no zone-center modes at these frequencies, so we assign these features as arising from multi-phonon Raman scattering processes. The large number of Raman-active, single-phonon modes makes it difficult to determine which vibrations are involved in generating these peaks, however we note that the 735 cm^{-1} mode is unique from the others as it exhibits B_{1g} symmetry.

Experiment (cm^{-1})	Symmetry
468	A_{1g}
638	A_{1g}
735	B_{1g}
842	A_{1g}

Table 2: Experimentally-observed multi-phonon Raman modes.

6. Discussion

Chalcogenide perovskites have crystal structures and large dielectric susceptibility in common with halide and oxide perovskites [14]. However, chalcogenides feature substantially more covalent bonding between the metal (M) and anion (X) than do the more ionic halides and oxides. This more directional bonding means that the M-X-M bond angles have an amplified effect on the electronic structure. In perovskite oxides, bond angles control correlation effects via the bandwidth [39,40]. In perovskite chalcogenides, bond angles control the semiconductor band gap and the low-energy electronic structure at the band edges.

We highlight in **Fig. 8** the connections between polarized XANES spectroscopy, electronic structure calculations, and semiconducting functionality of $Ba_3Zr_2S_7$. $Ba_3Zr_2S_7$ has a reduced band gap relative to $BaZrS_3$ due to the increased covalency of the Zr-S-Zr bonding network among corner-sharing octahedra in the basal plane [10]. To interpret the A' and A features in detail, we focus on the orbital-resolved contributions to the band structure of $Ba_3Zr_2S_7$ as calculated by DFT. In **Fig. 8a-b**, we show the contributions of relevant S and Zr orbitals to the low energy electronic structure, as identified by S K-edge and Zr L-edge XANES. We start the plot from the conduction band minimum, as XANES does not probe the valence band. Although these band structure plots do not consider matrix elements, the presence of unoccupied states in the conduction band is a necessary requirement for the XANES features seen in **Fig. 5**, in a straightforward interpretation of Fermi's golden rule. For the S3p orbitals, we show only the equatorial and bilayer sites, as the calculated interface site contribution to the overall XANES spectra is minor (see **Fig. 5f-g**). We find that the lowest-energy feature, A', derives primarily from $Zr4d_{xy}$ and bilayer $S3p_{x/y}$ orbitals at the conduction band minimum. For small θ, the X-ray electric field vector ($\underline{E}$) lies in the basal plane and is effective at promoting dipole transitions between the S1s core levels and conduction band states comprised of Zr4d_{xy} – bilayer S3$p_{x/y}$ π^* bonds. At higher energies (approximately 1.5 – 2.0 eV above the conduction band minimum), the A feature dominates the XANES spectrum, which correlates with changes in the calculated contributions from Zr4$d_{xz/yz}$, Zr4d_{xy}, equatorial S3$p_{x/y}$, and equatorial S3p_z orbitals. For large θ, $\underline{E}$ is directed along the c axis and is effective at promoting transitions to conduction band states with S3p_z character. In summary, our analysis indicates that the A' and A features in the S K-edge spectra derive from covalent π^* bonds between Zr4d orbitals and the 3p orbitals of bilayer and equatorial sulfur sites. The resulting bands are strongly dispersive in-plane: see for instance the $\Gamma - M$ trajectories in **Fig. 8a-b**, and the delocalized electron density in **Fig. 8c**. This dispersion results from covalent bonding, and is responsible for the decreased band gap in $Ba_3Zr_2S_7$ relative to $BaZrS_3$, and for the high charge transport mobility that we infer here from IR reflectivity.

In **Fig. 8c-d**, we show the projected electron density distributions in $Ba_3Zr_2S_7$ as slices of the (001) and (010) planes, as calculated by DFT. These distributions correspond to an energy band at the conduction band minimum that contains substantial contributions from the 3p orbitals of both equatorial and bilayer sulfur sites. The charge density maps clearly portray the covalent bonding network between Zr4d and S3p orbitals, and the charge delocalization within layers of the layered crystal structure. Both the Zr4d and equatorial S3p orbitals are strongly hybridized. The Zr4d orbitals appear to have both d_{xy} and $d_{xz/yz}$ character, while the equatorial S3p orbitals are a mix of p_x, p_y, and p_z. Bands near the conduction band minimum all have t_{2g} character at the Zr sites, whereas bands with e_g character are found at higher energy. This is consistent with the ordering of π^* and σ^* bonds expected from crystal field theory, and with our analysis of the Zr L_2-edge spectra (**Fig. 2**), and again highlights the interesting balance between covalent and ionic bonding found in the chalcogenide perovskites.

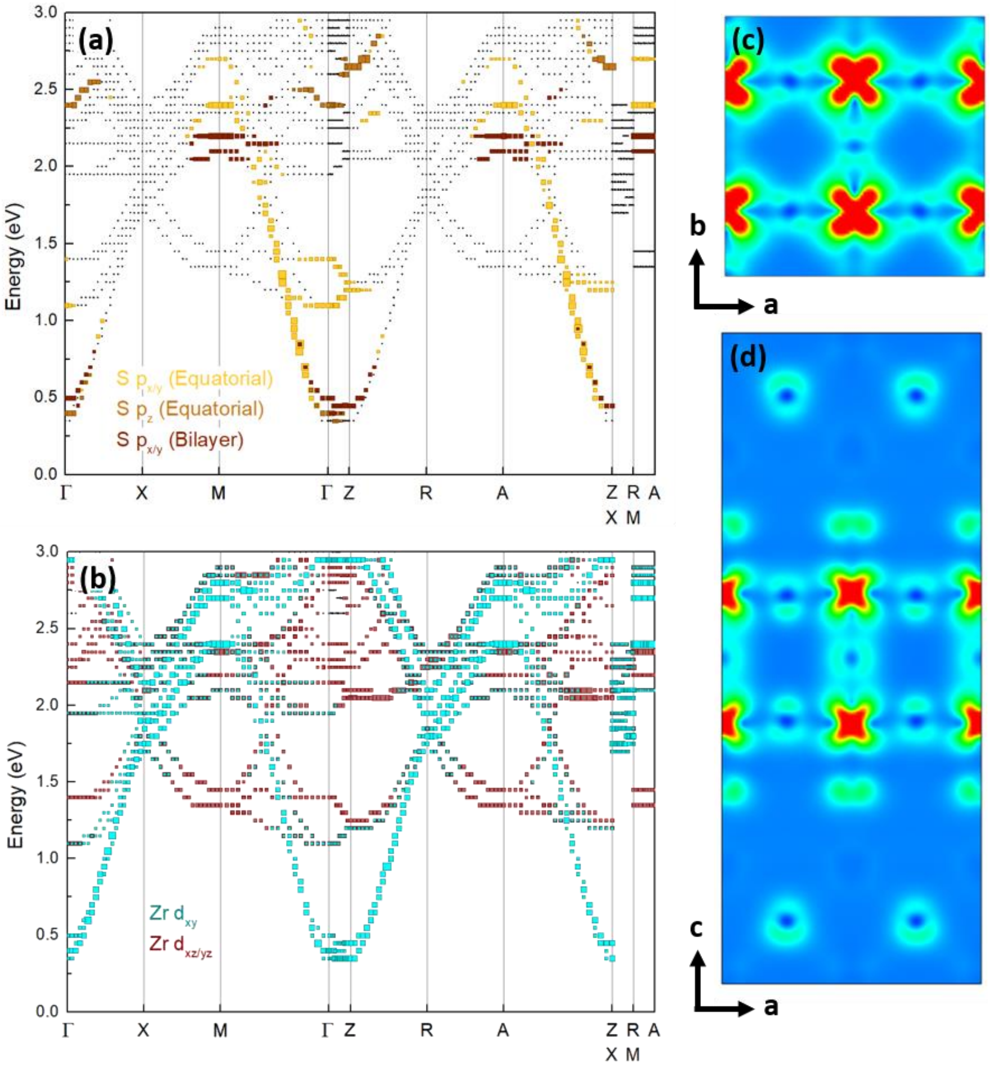

Figure 8: Low-energy electronic structure of the conduction band and projected electron density distributions of the semiconductor $Ba_3Zr_2S_7$ in the layered, Ruddlesden-Popper structure. Bands are colored according to their dominant orbital character, showing sulfur orbitals in (a) and zirconium orbitals in (b). The dotted lines illustrate the overall band structure, with colored markers representing the relative contribution of each orbital at a given point in Brillouin zone. (a) Sulfur 3p orbital contributions from equatorial and bilayer sulfur sites. (b) Zr 4d orbital contributions. (c, d) Projected electron density distributions for an energy band at the conduction band minimum, highlighting the π^* bonding between Zr4d and S3p orbitals, shown as slices of the (001) and (010) planes in (c) and (d), respectively.

Our IR reflectivity measurements and DFT calculations are in qualitative agreement that there is as large difference between in-plane and out-of-plane charge transport mobility, but quantitatively they differ substantially. This highlights the need for a theoretical assessment of quasiparticles and charge transport in highly-polarizable semiconductors. Charge carriers in chalcogenide perovskites may be large polarons, due to the high low-frequency dielectric constant and large Fröhlich coupling constant and Pekar factor [14]. Phonons that affect bond angles and octahedral distortions are likely to couple strongly to band-edge states and contribute to polaron formation. Our DFT calculations presented here do not model excited-state charge transport in the presence of strong electron-phonon coupling; these effects should be explored in the future to reconcile the transport discrepancies. The large mobility values measured here are particularly interesting. Strong electron-phonon coupling and polaron quasiparticles are often associated with low charge transport mobility, such as diffusive transport in $SrTiO_3$ [41]. Our results suggest that charge transport may be quite different in chalcogenide perovskites than in their oxide relatives. Further experimental and theoretical studies of charge transport are left to future work.

7. Conclusion

In conclusion, we use a suite of experimental and theoretical methods to study electronic and structural properties of chalcogenides in the Ba-Zr-S system in the distorted-perovskite and Ruddlesden-Popper structure types. We find that the low-energy electronic structure (*i.e.* electronic properties near the band edges) is keenly sensitive to the degree of hybridization and covalent bonding between Zr4d and S3p orbitals, which we attribute to the established Zr-S-Zr bond angles in these materials [10]. This is expected for a covalent semiconductor, but is less-studied scientific territory for materials in the perovskite and related crystal structures. The relationships between the crystal chemistry and the low-energy electronic structure are illuminated by a combination of experimental and theoretical spectroscopic tools, including theoretical methods that can assign calculated X-ray absorption spectra to individual atomic sites and orbitals, enabling the clear identification of features in experimental data including polarized XANES. Our results highlight a network of S3p-Zr4d π^* bonds that are responsible for the dispersive conduction band, the reduced band gap vis-à-vis $BaZrS_3$, the strong optical absorption near the band edge, and fast charge transport. Our results suggest exciting directions to further study charge transport in highly-polarizable chalcogenide semiconductors.

Appendix A: Modeling visible-pump, IR probe experiments

The carrier-injection pulse is very fast relative to the previously-measured electron-hole recombination rates in $Ba_3Zr_2S_7$, and therefore we assume it is near-instantaneous [8]. Under this assumption, the instantaneous carrier generation profile through the crystal is:

$$n(x) = (1 - R)\alpha_{\mathrm{VIS}}\, F(x) = (1 - R_{\mathrm{VIS}})\alpha_{\mathrm{VIS}} 2F_0 e^{-\alpha_{\mathrm{VIS}} x} \tag{6}$$

R_{VIS} is the reflectivity at the sample-air interface at λ_{VIS}, α_{VIS} is the absorption coefficient at λ_{VIS}, $F(x) = F_0 e^{-\alpha_{\mathrm{VIS}} x}$ is the instantaneous incident photon areal density, x is the depth through the crystal, and F_0 is the total pump fluence. The factor of 2 comes from the assumption of ambipolar transport. For our experiments, $F_0 = 2.15 \times 10^{11}$ cm^{-2}. We estimate $R_{\mathrm{VIS}} = 24.8\%$ and $\alpha_{\mathrm{VIS}} = 1.27 \times 10^5$ cm^{-1} for $\lambda_{\mathrm{VIS}} = 515$ nm as predicted by theory [8]. In **Fig. A1a** we present the calculated instantaneous generation profile.

The frequency-dependent Drude conductivity is

$$\sigma = \frac{nq^2}{m^*}\frac{i}{\omega + i\Gamma} \tag{7}$$

Γ is the carrier scattering rate. The low-frequency limit $\omega_{IR} \ll \Gamma$ corresponds to assuming that the scattering rate is much faster than the probe frequency. In this limit, the dielectric constant (in Gaussian c.g.s. units) is

$$\varepsilon = \varepsilon_\infty + \frac{4\pi i n q \mu}{\omega} \tag{8}$$

ε_∞ is the equilibrium dielectric constant at the probe frequency, which is $\mathcal{O}(10\varepsilon_0)$ for the materials in question [14]. In **Fig. A1b** we compare the Drude response to $\varepsilon_\infty/\varepsilon_0 = 10$; we find that the Drude term is likely to be small relative to ε_∞ for a reasonable range of $\mu = 3 - 3 \times 10^5$ cm^2/statV/s = $0.01 - 1{,}000$ cm^2/V/s and for values of n as shown in **Fig. A1a**.

In the zero-frequency limit, the Drude mobility is $\mu = q/m^*\Gamma$. We plot in **Fig. A1c** the function $\Gamma = q/m^*\mu$ for reasonable ranges of m^* and μ. We find that the low-frequency assumption $\omega_{IR} \ll \Gamma$ is a good one.

The IR loss coefficient k is found from the IR dielectric constant according to $\sqrt{\varepsilon} = n + ik$. We expand the square root for $\frac{4\pi i n q \mu}{\omega} \ll \varepsilon_\infty$ and find

$$\sqrt{\varepsilon} \approx \sqrt{\varepsilon_\infty} + \frac{1}{2\sqrt{\varepsilon_\infty}} \frac{4\pi i n q \mu}{\omega} = n + ik \tag{9}$$

$$k = \frac{1}{2\sqrt{\varepsilon_\infty}} \times \frac{4\pi n q \mu}{\omega} \tag{10}$$

The absorption coefficient is then

$$\alpha_{IR} = \frac{2\omega}{c} k = \frac{4\pi n q \mu}{c\sqrt{\varepsilon_\infty}} \tag{11}$$

With transient carrier injection (*e.g.* **Fig. A1a**), α_{IR} is depth-dependent:

$$\alpha_{IR}(x) = c_1 \exp(-\alpha_{\mathrm{VIS}} x),\ c_1 = \frac{4\pi q \mu}{c\sqrt{\varepsilon_\infty}} (1 - R_{\mathrm{VIS}}) \alpha_{\mathrm{VIS}} 2F_0 \tag{12}$$

The differential equation describing the IR beam attenuation is of the form

$$\frac{\mathrm{d}I_{\mathrm{IR}}}{\mathrm{d}x} = -\alpha_{IR}(x) I_{\mathrm{IR}}(x) \tag{13}$$

This can be solved by separation:

$$I_{\mathrm{IR}}(x) = c_2 \exp\left[-\int dx' \alpha_{IR}(x')\right] \tag{14}$$

$$\int dx' \alpha_{IR}(x') = -\frac{c_1}{\alpha_{\mathrm{VIS}}} e^{-\alpha_{\mathrm{VIS}} x} \tag{15}$$

We normalize such that $I_{\mathrm{IR}}(x = 0) = 1$ to find $c_2 = \exp\left(-\frac{c_1}{\alpha_{\mathrm{VIS}}}\right)$, such that the final expression for $I_{\mathrm{IR}}(x)$ becomes:

$$I_{\mathrm{IR}}(x) = \exp\left(-\frac{c_1}{\alpha_{\mathrm{VIS}}}\right) \exp\left[\frac{c_1}{\alpha_{\mathrm{VIS}}} e^{-\alpha_{\mathrm{VIS}} x}\right],\ c_1 = \frac{4\pi q \mu}{c\sqrt{\varepsilon_\infty}} (1 - R_{\mathrm{VIS}}) \alpha_{\mathrm{VIS}} 2F_0 \tag{16}$$

We can define the skin depth δ_{IR} as the depth at which the IR probe beam is attenuated by e^{-1}. Using Eqn. 11 we can solve for δ_{IR}:

$$\delta_{\mathrm{IR}} = -\frac{1}{\alpha_{\mathrm{VIS}}} \ln\left(1 - {}^{\alpha_{\mathrm{VIS}}}\!/_{c_1}\right) \tag{17}$$

A condition for δ_{IR} to be real is that ${}^{\alpha_{\mathrm{VIS}}}\!/_{c_1} < 1$. If this isn't satisfied, then the IR probe beam is never attenuated by e^{-1}. For the parameters of our experiment, we find that δ_{IR} calculated using Eqn. 12 is imaginary, meaning that the IR probe beam is not strongly attenuated. This can be seen clearly from a plot of $I_{\mathrm{IR}}(x)$ for our experimental parameters and a reasonable choice of $\mu = 10\ \mathrm{cm}^2/\mathrm{V}/\mathrm{s}$, shown in **Fig. A1d**.

Fig. A1d shows that the IR beam is attenuated only by a thin, conductive layer at the sample surface under illumination. For this layer of thickness d, where $d \ll \delta_{\mathrm{IR}}$ and $d \ll \lambda_{\mathrm{IR}}$, we can use the sheet conductivity approximation [42]. In this approximation, the IR reflectivity is

$$R = \frac{(y_1+n-1)^2+y_2^2}{(y_1+n+1)^2+y_2^2},\ y = y_1 + iy_2 = Z_0(\sigma_1 + i\sigma_2)d \tag{18}$$

$Z_0 = 4\pi/c$ is the impedance of free space. In the low-frequency limit (see above), $y_1 = Z_0\sigma_1 d$ and $\sigma_2 = y_2 = 0$. In this case:

$$R = \frac{(y_1+n-1)^2}{(y_1+n+1)^2} \tag{19}$$

For $\alpha_{\mathrm{VIS}}^{-1} \ll \delta$, then we can assume all incident pump light (that which isn't reflected) is absorbed within the thin conductive sheet: $nd = (1 - R_{\mathrm{VIS}})2F_0$, $\sigma_1 d = q\mu(1 - R_{\mathrm{VIS}})2F_0$, $y_1 = Z_0 q\mu(1 - R_{\mathrm{VIS}})2F_0$. For the parameters of our experiment we have $y_1 \ll n$, and Eqn. 19 can be expanded to yield Eqn. 3.

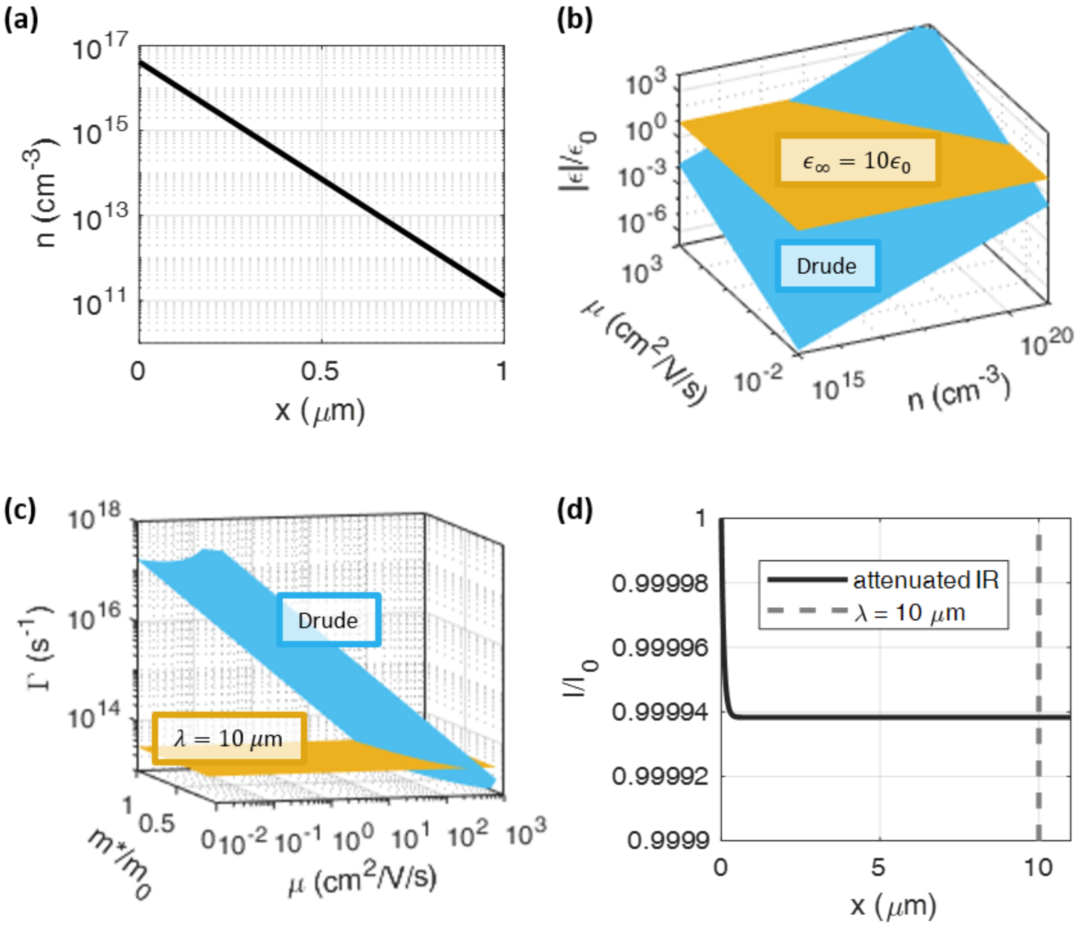

Figure A1: Evaluating model for analysis of visible-pump, IR probe experiments. (a) Instantaneous carrier injection as a function of position through the sample with experimental parameters, with the front face at $x = 0$. (b) Comparing the Drude response (magnitude of complex dielectric constant) to $10\epsilon_0$; for all reasonable combination of carrier concentration n and mobility μ, the Drude response is small compared to $10\epsilon_0$. (c) Comparing the Drude model scattering rate to the frequency of the IR probe. For all reasonable combination of μ and carrier effective mass m^*/m_0 (where m_0 is the free electron mass), the IR probe is in the low-frequency limit. (d) IR probe beam attenuation for experimental parameters and a reasonable choice for $\mu = 10\ \mathrm{cm}^2/\mathrm{V/s}$. The IR beam is only weakly attenuated. The layer of thickness d responsible for IR attenuation is much smaller than the IR skin depth ($d \ll \delta_{\mathrm{IR}}$) and also much smaller than the IR wavelength ($d \ll \lambda_{\mathrm{IR}}$).

Acknowledgements

We acknowledge support from the National Science Foundation (NSF) under grant no. 1751736, "CAREER: Fundamentals of Complex Chalcogenide Electronic Materials." A portion of this project was funded by the Skolkovo Institute of Science and Technology as part of the MIT-Skoltech Next Generation Program. K. Y. acknowledges support by the NSF Graduate Research Fellowship, grant no. 1745302. S. N., B. Z., and J. R. acknowledge the support from the Army Research Office under Award numbers W911NF-19-1-0137 and W911NF-21-0327, and the University of Southern California Provost New Strategic Directions for Research Award. A.S. acknowledges support by the National Science Foundation under grant no. DMR-1555153. P.M.V. and A.J.R. acknowledge support from the NSF under grant no. 1847782, “CAREER: Proximity Effects in van der Waals Heterostructures”. N.Z.K. and J.M.R. were supported by NSF Grant No. DMR-2011208. Use of the Stanford Synchrotron Radiation Lightsource, SLAC National Accelerator Laboratory, is supported by the U.S. Department of Energy, Office of Science, Office of Basic Energy Sciences under Contract No. DE-AC02-76SF00515. A.B. acknowledges support by the state of Baden-Württemberg through bwHPC and the German Research Foundation (DFG) through grant no INST 40/575-1 FUGG (JUSTUS 2 cluster). DFT calculations used the Extreme Science and Engineering Discovery Environment (XSEDE), which is supported by the National Science Foundation under Grant No. ACI-1548562 and the National Energy Research Scientific Computing Center (NERSC), a U.S. DOE Office of Science User Facility located at Lawrence Berkeley National Laboratory, operated under Contract No. DE-AC02-05CH11231.

References

[1] Z. Yu, X. Wei, Y. Zheng, H. Hui, M. Bian, S. Dhole, J.-H. Seo, Y.-Y. Sun, Q. Jia, S. Zhang, S. Yang, and H. Zeng, *Chalcogenide Perovskite BaZrS3 Thin-Film Electronic and Optoelectronic Devices by Low Temperature Processing*, Nano Energy **85**, 105959 (2021).

[2] J. A. Márquez, M. Rusu, H. Hempel, I. Y. Ahmet, M. Kölbach, I. Simsek, L. Choubrac, G. Gurieva, R. Gunder, S. Schorr, and T. Unold, *BaZrS3 Chalcogenide Perovskite Thin Films by H2S Sulfurization of Oxide Precursors*, The Journal of Physical Chemistry Letters **12**, 2148 (2021).

[3] T. Gupta, D. Ghoshal, A. Yoshimura, S. Basu, P. K. Chow, A. S. Lakhnot, J. Pandey, J. M. Warrender, H. Efstathiadis, A. Soni, E. Osei- Agyemang, G. Balasubramanian, S. Zhang, S.-F. Shi, T.-M. Lu, V. Meunier, and N. Koratkar, *An Environmentally Stable and Lead-Free Chalcogenide Perovskite*, Advanced Functional Materials **30**, 2001387 (2020).

[4] X. Wei, H. Hui, C. Zhao, C. Deng, M. Han, Z. Yu, A. Sheng, P. Roy, A. Chen, J. Lin, D. F. Watson, Y.-Y. Sun, T. Thomay, S. Yang, Q. Jia, S. Zhang, and H. Zeng, *Realization of BaZrS3 Chalcogenide Perovskite Thin Films for Optoelectronics*, Nano Energy **68**, 104317 (2020).

[5] C. Comparotto, A. Davydova, T. Ericson, L. Riekehr, M. V. Moro, T. Kubart, and J. Scragg, *Chalcogenide Perovskite BaZrS3: Thin Film Growth by Sputtering and Rapid Thermal Processing*, ACS Appl. Energy Mater. (2020).

[6] Y. Nishigaki, T. Nagai, M. Nishiwaki, T. Aizawa, M. Kozawa, K. Hanzawa, Y. Kato, H. Sai, H. Hiramatsu, H. Hosono, and H. Fujiwara, *Extraordinary Strong Band-Edge Absorption in Distorted Chalcogenide Perovskites*, Solar RRL **4**, 1900555 (2020).

[7] K. Hanzawa, S. Iimura, H. Hiramatsu, and H. Hosono, *Material Design of Green-Light-Emitting Semiconductors: Perovskite-Type Sulfide SrHfS3*, J. Am. Chem. Soc. **141**, 5343 (2019).

[8] S. Niu, D. Sarkar, K. Williams, Y. Zhou, Y. Li, E. Bianco, H. Huyan, S. B. Cronin, M. E. McConney, R. Haiges, R. Jaramillo, D. J. Singh, W. A. Tisdale, R. Kapadia, and J. Ravichandran, *Optimal Bandgap in a 2D Ruddlesden–Popper Perovskite Chalcogenide for Single-Junction Solar Cells*, Chem. Mater. **30**, 4882 (2018).

[9] S. Niu, H. Huyan, Y. Liu, M. Yeung, K. Ye, L. Blankemeier, T. Orvis, D. Sarkar, D. J. Singh, R. Kapadia, and J. Ravichandran, *Bandgap Control via Structural and Chemical Tuning of Transition Metal Perovskite Chalcogenides*, Adv. Mater. **29**, 1604733 (2017).

[10] W. Li, S. Niu, B. Zhao, R. Haiges, Z. Zhang, J. Ravichandran, and A. Janotti, *Band Gap Evolution in Ruddlesden-Popper Phases*, Phys. Rev. Materials **3**, 101601 (2019).

[11] S. Niu, J. Milam-Guerrero, Y. Zhou, K. Ye, B. Zhao, B. C. Melot, and J. Ravichandran, *Thermal Stability Study of Transition Metal Perovskite Sulfides*, Journal of Materials Research **33**, 4135 (2018).

[12] V. K. Ravi, S. H. Yu, P. K. Rajput, C. Nayak, D. Bhattacharyya, D. S. Chung, and A. Nag, *Colloidal BaZrS3 Chalcogenide Perovskite Nanocrystals for Thin Film Device Fabrication*, Nanoscale **13**, 1616 (2021).

[13] R. Jaramillo and J. Ravichandran, *In Praise and in Search of Highly-Polarizable Semiconductors: Technological Promise and Discovery Strategies*, APL Materials **7**, 100902 (2019).

[14] S. Filippone, B. Zhao, S. Niu, N. Z. Koocher, D. Silevitch, I. Fina, J. M. Rondinelli, J. Ravichandran, and R. Jaramillo, *Discovery of Highly Polarizable Semiconductors BaZrS3 and Ba3Zr2S7*, Phys. Rev. Materials **4**, 091601 (2020).

[15] M. Surendran, H. Chen, B. Zhao, A. S. Thind, S. Singh, T. Orvis, H. Zhao, J.-K. Han, H. Htoon, M. Kawasaki, R. Mishra, and J. Ravichandran, *Epitaxial Thin Films of a Chalcogenide Perovskite*, ArXiv:2105.11090 [Cond-Mat] (2021).

[16] I. Sadeghi, K. Ye, M. Xu, Y. Li, J. M. LeBeau, and R. Jaramillo, *Making BaZrS3 Chalcogenide Perovskite Thin Films by Molecular Beam Epitaxy*, Advanced Functional Materials **31**, 2105563 (2021).

[17] S. Niu, B. Zhao, K. Ye, E. Bianco, J. Zhou, M. E. McConney, C. Settens, R. Haiges, R. Jaramillo, and J. Ravichandran, *Crystal Growth and Structural Analysis of Perovskite Chalcogenide BaZrS3 and Ruddlesden–Popper Phase Ba3Zr2S7*, Journal of Materials Research **34**, 3819 (2019).

[18] B. Ravel and M. Newville, ATHENA , ARTEMIS , HEPHAESTUS *: Data Analysis for X-Ray Absorption Spectroscopy Using* IFEFFIT, J Synchrotron Rad **12**, 537 (2005).

[19] G. Kresse and J. Furthmüller, *Efficient Iterative Schemes for Ab Initio Total-Energy Calculations Using a Plane-Wave Basis Set*, Phys. Rev. B **54**, 11169 (1996).

[20] G. Kresse and D. Joubert, *From Ultrasoft Pseudopotentials to the Projector Augmented-Wave Method*, Phys. Rev. B **59**, 1758 (1999).

[21] J. P. Perdew, A. Ruzsinszky, G. I. Csonka, O. A. Vydrov, G. E. Scuseria, L. A. Constantin, X. Zhou, and K. Burke, *Restoring the Density-Gradient Expansion for Exchange in Solids and Surfaces*, Phys. Rev. Lett. **100**, 136406 (2008).

[22] F. Karsai, M. Humer, E. Flage-Larsen, P. Blaha, and G. Kresse, *Effects of Electron-Phonon Coupling on Absorption Spectrum: K Edge of Hexagonal Boron Nitride*, Phys. Rev. B **98**, 235205 (2018).

[23] M. Gajdoš, K. Hummer, G. Kresse, J. Furthmüller, and F. Bechstedt, *Linear Optical Properties in the Projector-Augmented Wave Methodology*, Phys. Rev. B **73**, 045112 (2006).

[24] J. Leveillee, C. Katan, L. Zhou, A. D. Mohite, J. Even, S. Tretiak, A. Schleife, and A. J. Neukirch, *Influence of Pi-Conjugated Cations and Halogen Substitution on the Optoelectronic and Excitonic Properties of Layered Hybrid Perovskites*, Phys. Rev. Materials **2**, 105406 (2018).

[25] J. M. Skelton, L. A. Burton, A. J. Jackson, F. Oba, S. C. Parker, and A. Walsh, *Lattice Dynamics of the Tin Sulphides SnS2, SnS and Sn2S3: Vibrational Spectra and Thermal Transport*, Phys. Chem. Chem. Phys. **19**, 12452 (2017).

[26] A. Togo and I. Tanaka, *First Principles Phonon Calculations in Materials Science*, Scripta Materialia **108**, 1 (2015).

[27] P. V. C. Medeiros, S. Stafström, and J. Björk, *Effects of Extrinsic and Intrinsic Perturbations on the Electronic Structure of Graphene: Retaining an Effective Primitive Cell Band Structure by Band Unfolding*, Phys. Rev. B **89**, 041407 (2014).

[28] P. V. C. Medeiros, S. S. Tsirkin, S. Stafström, and J. Björk, *Unfolding Spinor Wave Functions and Expectation Values of General Operators: Introducing the Unfolding-Density Operator*, Phys. Rev. B **91**, 041116 (2015).

[29] O. Bunău and Y. Joly, *Self-Consistent Aspects of x-Ray Absorption Calculations*, J. Phys.: Condens. Matter **21**, 345501 (2009).

[30] S. A. Guda, A. A. Guda, M. A. Soldatov, K. A. Lomachenko, A. L. Bugaev, C. Lamberti, W. Gawelda, C. Bressler, G. Smolentsev, A. V. Soldatov, and Y. Joly, *Optimized Finite Difference Method for the Full-Potential XANES Simulations: Application to Molecular Adsorption Geometries in MOFs and Metal–Ligand Intersystem Crossing Transients*, J. Chem. Theory Comput. **11**, 4512 (2015).

[31] A. Grechnev, R. Ahuja, and O. Eriksson, *Balanced Crystal Orbital Overlap Population—a Tool for Analysing Chemical Bonds in Solids*, J. Phys.: Condens. Matter **15**, 7751 (2003).

[32] J. Suntivich, W. T. Hong, Y.-L. Lee, J. M. Rondinelli, W. Yang, J. B. Goodenough, B. Dabrowski, J. W. Freeland, and Y. Shao-Horn, *Estimating Hybridization of Transition Metal and Oxygen States in Perovskites from O K-Edge X-Ray Absorption Spectroscopy*, J. Phys. Chem. C **118**, 1856 (2014).

[33] K. W. Böer, *Handbook of the Physics of Thin-Film Solar Cells*, 2013 edition (Springer, New York, 2014).

[34] M. Powalla, S. Paetel, E. Ahlswede, R. Wuerz, C. D. Wessendorf, and T. Magorian Friedlmeier, *Thin‐ film Solar Cells Exceeding 22% Solar Cell Efficiency: An Overview on CdTe-, Cu(In,Ga)Se2-, and Perovskite-Based Materials*, Applied Physics Reviews **5**, 041602 (2018).

[35] M. Ishii, M. Saeki, and M. Sekita, *Vibrational Spectra of Barium-Zirconium Sulfides*, Materials Research Bulletin **28**, 493 (1993).

[36] M. I. Aroyo, J. M. Perez-Mato, C. Capillas, E. Kroumova, S. Ivantchev, G. Madariaga, A. Kirov, and H. Wondratschek, *Bilbao Crystallographic Server: I. Databases and Crystallographic Computing Programs*, Zeitschrift Für Kristallographie - Crystalline Materials **221**, 15 (2006).

[37] M. I. Aroyo, A. Kirov, C. Capillas, J. M. Perez-Mato, and H. Wondratschek, *Bilbao Crystallographic Server. II. Representations of Crystallographic Point Groups and Space Groups*, Acta Cryst A **62**, 2 (2006).

[38] C. Franchini, M. Reticcioli, M. Setvin, and U. Diebold, *Polarons in Materials*, Nat Rev Mater **6**, 560 (2021).

[39] J. B. Goodenough, *Metallic Oxides*, Progress in Solid State Chemistry **5**, 145 (1971).

[40] R. Jaramillo, S. D. Ha, D. M. Silevitch, and S. Ramanathan, *Origins of Bad-Metal Conductivity and the Insulator-Metal Transition in the Rare-Earth Nickelates*, Nat Phys **10**, 304 (2014).

[41] J.-J. Zhou and M. Bernardi, *Predicting Charge Transport in the Presence of Polarons: The beyond-Quasiparticle Regime in SrTiO3*, Phys. Rev. Research **1**, 033138 (2019).

[42] F. Gao, G. L. Carr, C. D. Porter, D. B. Tanner, G. P. Williams, C. J. Hirschmugl, B. Dutta, X. D. Wu, and S. Etemad, *Quasiparticle Damping and the Coherence Peak in YBa2Cu3O7-δ*, Phys. Rev. B **54**, 700 (1996).